Supporting Information: Thermal and ablation properties of a high-entropy metal diboride:$(Hf_{0.2}Zr_{0.2}Ti_{0.2}Ta_{0.2}Nb_{0.2})B_2$

Md Shafkat Bin Hoque, Milena Milich, Md Sabbir Akhanda, Sashank Shivakumar, Eric R. Hoglund, Dragos Staicu, Mingde Qin, Kathleen F. Quiambao-Tomko, John A. Tomko, Jeffrey L. Braun, Joshua Gild, David H. Olson, Kiumars Aryana, Yee Rui Koh, Roisul Galib, Luka Vlahovic, Davide Robba, John T. Gaskins, Mona Zebarjadi, Jian Luo, and Patrick E. Hopkins

Md Shafkat Bin Hoque, Milena Milich, John A. Tomko, Kiumars Aryana, Yee Rui Koh, Roisul Galib
Department of Mechanical and Aerospace Engineering, University of Virginia, Charlottesville, Virginia 22904, USA

Md Sabbir Akhanda, Mona Zebarjadi
Department of Electrical Engineering, University of Virginia, Charlottesville, Virginia 22904, USA

Sashank Shivakumar, Mingde Qin, Joshua Gild, Jian Luo
Materials Science and Engineering Program, University of California San Diego, La Jolla, CA, 92093, USA

Eric R. Hoglund, Kathleen F. Quiambao-Tomko
Department of Materials Science and Engineering, University of Virginia, Charlottesville, Virginia 22904, USA

Dragos Staicu, Luka Vlahovic, Davide Robba
European Commission, Joint Research Centre, Institute for Transuranium Elements, P.O. Box 2340, D-76125 Karlsruhe, Germany

Jeffrey L. Braun, David H. Olson, John T. Gaskins
Laser Thermal Analysis, Charlottesville, Virginia 22902, USA

Patrick E. Hopkins
Department of Mechanical and Aerospace Engineering, University of Virginia, Charlottesville, Virginia 22904, USA
Department of Materials Science and Engineering, University of Virginia, Charlottesville, Virginia 22904, USA
Department of Physics, University of Virginia, Charlottesville, Virginia 22904, USA
Email: phopkins@virginia.edu

S1. Time-domain thermoreflectance (TDTR)

Time-domain thermoreflectance (TDTR) is a non-contact, optical, pump-probe technique that measures the thermal properties of a material by correlating the reflectance change with temperature.[1] The TDTR setup used in this study is of two-tint configuration,[2,3] in which a Ti:sapphire pulsed laser (central wavelength 808 nm and repetition rate 12.5 ns) is split into a pump and a probe path. The high-energy pump beam is modulated at a frequency of 8.4 MHz by an electro-optic modulator (EOM) and creates a periodic temperature oscillation at the sample surface. The resulting reflectance change is monitored by a time-delayed low-energy probe beam using a balanced photodetector and a lock-in amplifier. By fitting the ratio of in-phase to out-of-phase signal from the lock-in amplifier to a multilayer heat diffusion model,[4–6] the thermal properties of the sample are determined. Prior to the thermal measurements, a thin aluminum (Al) layer with a nominal thickness of 85 nm is deposited atop the sample surface via electron beam evaporation for optothermal transduction.[7] For the HEB heat capacity measurements, we use a 10X objective with $1/e^2$ pump and probe diameters of ∼22 and 11 μm, respectively. The uncertainty associated with the TDTR-measured heat capacity includes the measurement repeatability, uncertainty of the Al thickness (2 nm), and Al and HEB thermal conductivities (∼10%).

To spatially map the thermal conductivity with TDTR, we employ the same approach used by Olson *et al.*[3] A 2-axis stage is used to move the sample across the target region. During this movement, the ratio of in-phase to out-of-phase signal is collected at discrete points to create the pixels. By using the aforementioned heat diffusion model, thermal conductivity corresponding to each pixel is determined. Then by combining all the pixels together in an appropriate order, the thermal conductivity map of Figure S1 is generated. For the HEB mapping, we use a 20X objective with $1/e^2$ pump and probe diameters of ∼11 and 6 μm, respectively. The sample is moved from one end of the region to another using a step size of 1.25 μm. The probe delay time is kept fixed at 0.625 ns to minimize sensitivity to the Al/HEB thermal boundary conductance. The HEB thermal conductivity map corresponds to a heat capacity of 2.84 MJ m^{-3} K^{-1}. Some areas of these thermal conductivity map are affected by artifacts such as stray dust, debris, and nonspecular surfaces.

To determine which areas are affected by such artifacts, we depend on the auxiliary signals from the balanced photodetector. During TDTR measurements of a specular surface, the auxiliary signals from the reference and sample probe beams remain the same. However, due to diffusive scattering by the aforementioned artifacts, the auxiliary signals can differ between the two beams. Using a 95% threshold, we consider an area to be affected by scattering when this difference becomes greater than 5%. Such areas are excluded in the thermal conductivity distribution plots of Figure 3. Additional details regarding this methodology can be found elsewhere.[8]

To spatially map the ZrB_2, the same procedure is followed with a couple of changes. As the ZrB_2 grain size is 7.3 $\pm$ 4.2 μm, we use $1/e^2$ pump and probe radii of 4.4 μm for the mapping. Additionally, the probe delay time is kept fixed at 0.65 ns to minimize sensitivity to the Al/ZrB_2 thermal boundary conductance.

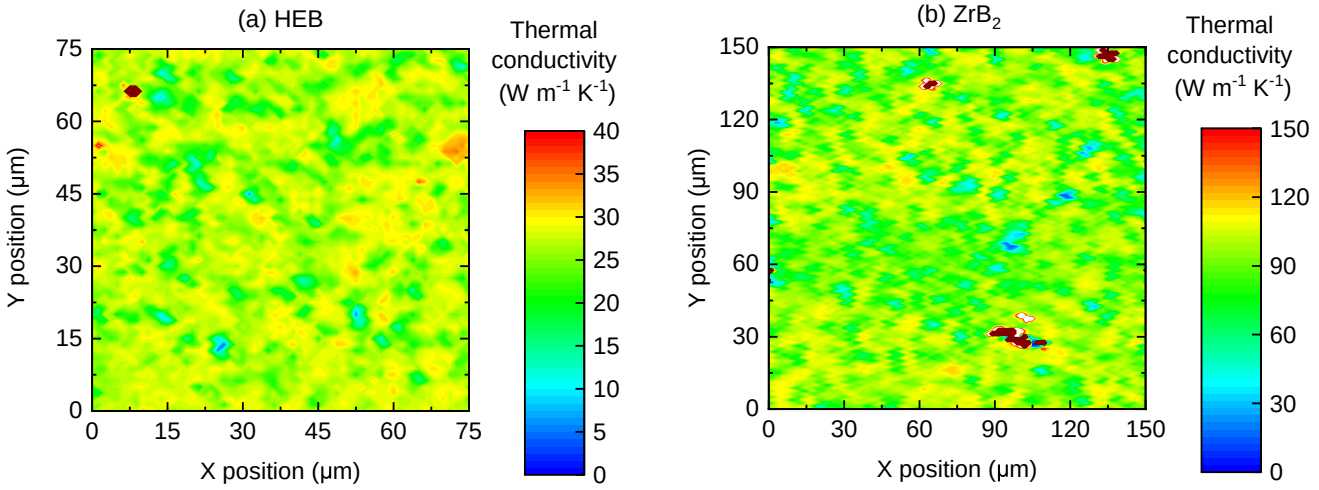

Figure S1: Thermal conductivity maps of (a) HEB and (b) ZrB_2.

S2. Steady-state thermoreflectance (SSTR)

The non-contact, optical, pump-probe technique steady-state thermoreflectance (SSTR) uses Fourier's law to determine the thermal conductivity of a material.[9] By varying the power from a 532 nm continuous wavelength (CW) pump laser, the incident heat flux at the sample surface is changed. At each pump power, the resultant reflectance change (proportional to the steady-state temperature rise) is detected by a 786 nm CW diode probe laser. By correlating the steady-state temperature rise with heat flux via an experimental proportionality constant, γ, the thermal conductivity of any material can be determined. A sapphire wafer is used as the reference sample for determining this γ constant according to the procedure detailed in Hoque *et al.*[7] In our SSTR setup, the coaxially focused $1/e^2$ pump and probe diameters are nearly equal, $\sim$20 μm. The SSTR measurements represent the geometric mean of in-plane and cross-plane thermal conductivities.[9] This is in contrast to TDTR, which represents measurements taken along the cross-plane direction. The uncertainty associated with the SSTR-measured value includes the repeatability of our measurements, uncertainty of the γ value, Al transducer thermal conductivity, and thermal boundary conductance.

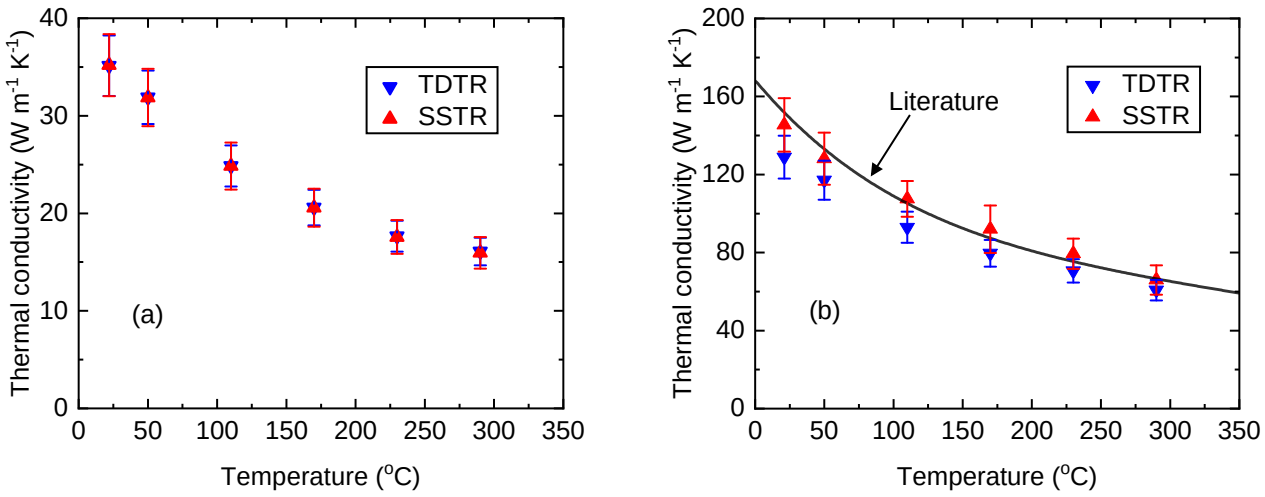

Figure S2: (a) TDTR-measured sapphire thermal conductivities (blue downward triangles) used as references for γ values. Using these γ values, the exhibited SSTR-measured sapphire thermal conductivities (red upward triangles) are obtained. (b) SSTR- and TDTR-measured Si thermal conductivity from room temperature to 290 °C. The solid line represents the literature[10] reported Si thermal conductivity.

Since SSTR is a relatively new technique, we use bulk silicon (Si) to calibrate it. Figure S2(b)

shows the Si thermal conductivities measured by both TDTR and SSTR from room temperature to 290 °C. As exhibited here, within uncertainty, the SSTR-measured values are in excellent agreement with literature.[10] The TDTR-measured values, on the other hand, are slightly lower than the literature reported Si thermal conductivities. Several recent studies[11–13] have reported that TDTR measurements of Si and other high thermal conductivity crystals can suffer from ballistic phonon transport, interfacial phonon-scattering, non-equilibrium processes, and heater length scales. We attribute these factors to be responsible for the lower Si thermal conductivities measured by TDTR.

S3. Laser Flash Analysis (LFA)

The laser flash method[14] using Netzsch LFA 467 is employed to measure the thermal diffusivity of the HEB at two different institutions: up to 475 °C at University of Virginia and up to 1267 °C at European Commission, Joint Research Centre, Karlsruhe. During the measurement, the front surface of a 2 mm thick HEB specimen is first heated by a short pulse of energy generated by a xenon lamp. Then, an infrared (IR) detector is used to measure the resulting time-dependent temperature rise on the rear surface of the sample. A thin layer of graphite is sprayed on the sample surface for enhanced absorption of energy emitted from the laser pulse.

S4. Electron backscatter diffraction (EBSD)

The grain orientations of the HEB and ZrB_2 are characterized through electron backscatter diffraction (EBSD)[15,16] conducted on a FEI Apreo microscope equipped with an Oxford Symmetry EBSD detector at an acceleration voltage of 20 kV and 26 nA. Data analysis is performed using the AZtecCrystal software suite. Samples are hot mounted in epoxy, ground and polished to a mirror finish prior to characterization. Final polishing is performed using colloidal silica. During EBSD, the samples are oriented such that the Normal Direction (ND) is parallel to the axis of applied pressure during sintering of both boride specimens. Scan step sizes of 0.7 and 1.5 μm are used for the ZrB_2 and HEB specimen, respectively. Statistics are taken from >3000 measured grains for each sample. Pole figures and disorientation angle distributions are obtained from the EBSD data.

S5. Elemental composition of the ZrB_2 specimen

The elemental composition of ZrB_2 is measured by energy dispersive X-ray spectroscopy (EDS) in a scanning electron microscope (SEM) and presented in Table S1. SEM-EDS is performed on a Thermo Fisher Scientific Helios dual-beam focused ion-beam equipped with an oxford X-Max 8 EDS detector. The acquisition conditions for the 2-minute continuous raster are 10 kV, 3.2 nA, and 300 ns/pixel. Carbon (C) and aluminum (Al) are excluded from the quantification results.

Table S1: The elemental compositions of the ZrB_2 specimen at two different positions.

Element	wt(%)	
	Position 1	Position 2
Zirconium (Zr)	92.29	93.33
Boron (B)	2.79	1.1
Oxygen (O)	3.81	4.93
Magnesium (Mg)	0.22	0.53
Titanium (Ti)	0.11	0.08
Strontium (Sr)	0.79	0.02

S6. Laser ablation threshold measurement

A schematic of our laser ablation setup is shown in Figure S3. In this setup, a ∼200 fs, 1040nm pulse emitted from a Ti:Sapphire laser is passed through a second harmonic generator, where it is converted to 520 nm. The converted beam has a Gaussian spatial profile as well as a Gaussian distribution in time. The beam is then focused using a 10X objective lens onto the sample surface and has a diameter of ∼17 um. Each ablation area shown in Figure 4(b) is damaged by this pulsed laser beam for 2 minutes using a 10 Hz pulse frequency, at a varied peak pulse power level. The diameter of the resultant damage is analyzed using image analysis software, ImageJ as well as SEM and plotted against the continuous-wave fluence equivalent used to generate the damage. The data is then fit with a logarithmic curve relating the known laser fluence to beam size and damage area, and extrapolated to determine at what laser fluence the material would initially exhibit damage. To ensure consistent absorption between the HEB and ZrB_2, the samples are first coated with ∼85 nm of aluminum. Once initial damage occurs, surface roughness scatters some of the laser light incident on the sample, but due to the depth of damage where the beam is incident, scattered light is trapped within the damage area and ultimately absorbed. Repeating the ablation measurements without any Al coating also generated nearly identical ablation threshold between the HEB and ZrB_2. The uncertainties of the measured ablation thresholds stem from the sparsity of experimental data points.

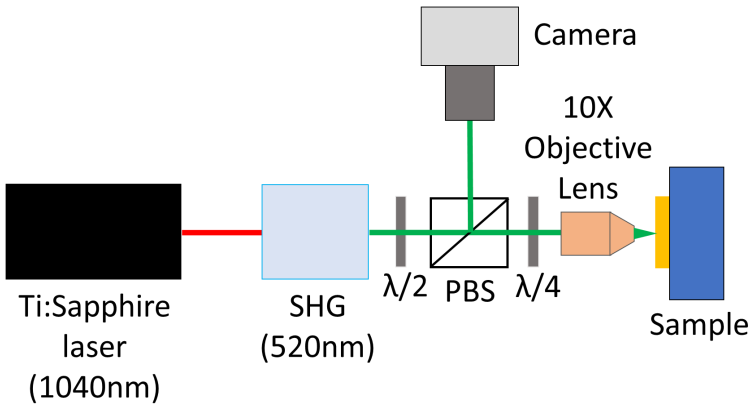

Figure S3: Schematic of the laser ablation setup. SHG: second harmonic generator, $\lambda/2$, $\lambda/4$: half- and quarter-wave plates, respectively, PBS: polarizing beam splitter.

S7. SEM images of HEB and ZrB_2

The SEM images of HEB and ZrB_2 are presented in Figure S4. The images are taken on a FEI Apreo microscope at acceleration voltages ranging from 5 to 10 kV and a beam current of 0.1 nA. Samples are hot mounted in epoxy, ground, and polished to a mirror finish prior to characterization. Final polishing is performed using colloidal silica.

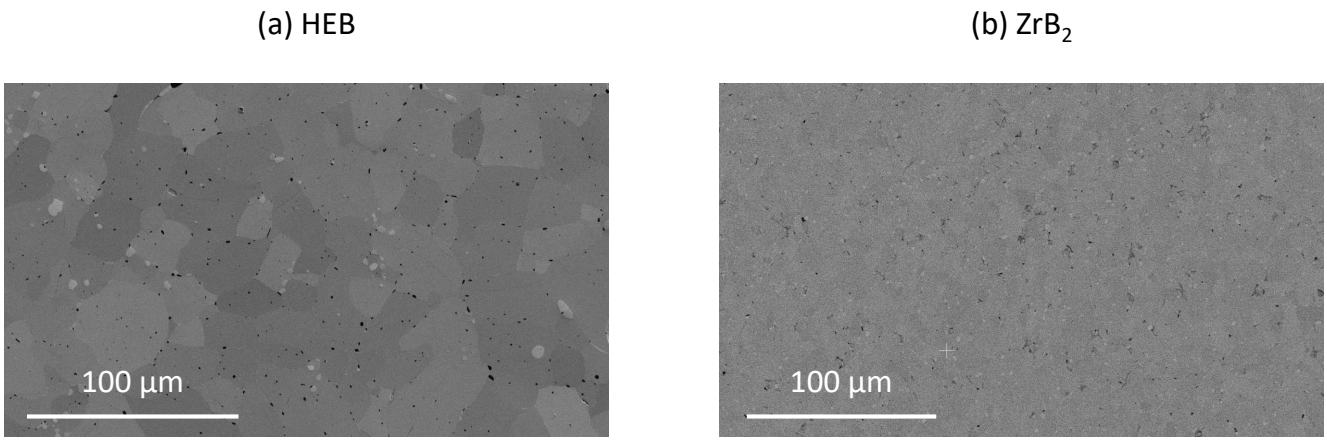

Figure S4: SEM images of (a) HEB and (b) ZrB_2.

S8. Scanning transmission electron microscopy (STEM) coupled with energy dispersive X-ray spectroscopy (EDS)

Plane view transmission electron microscopy samples are made using a Thermo Fisher Scientific Helios Dual Beam focused ion-beam. Ablated regions are filled with platinum to reduce uneven milling. Initial milling and cleaning are performed at 30 kV, after which it is sequentially decreased to a finishing energy of 5 kV. STEM-EDS is performed on a Thermo Fisher Scientific Themis-Z STEM operating at 200 kV with a 25 mrad convergence angle. EDS spectrum images are acquired with a 400 pA current and Super X EDS silicon drift detector system. Additional STEM and EDS images of the ablation areas on the HEB sample surface are provided in Figure S5.

As shown in Figure S5, the atomic number STEM images exhibit a constant contrast, which scales linearly with the TEM sample thickness. As a result, we assume constant thickness and absorption. We also include any absorption effects in the calculation. Therefore, the segregation affects observed are not expected to be influenced by either light or heavy atoms. This is validated by the fact that both niobium and boron are enriched in the same areas.

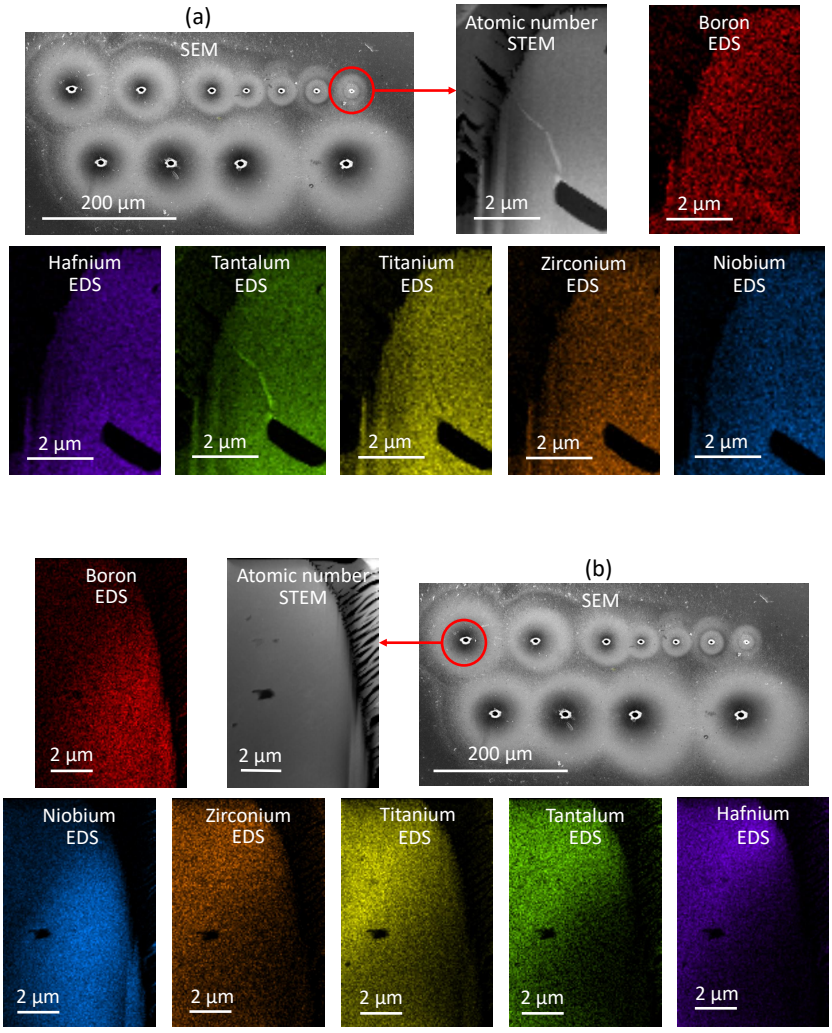

Figure S5: SEM, STEM, and EDS images of the ablation areas for the (a) small hole and (b) medium size hole.

References

[1] Jiang, P.; Qian, X.; Yang, R. Tutorial: Time-domain thermoreflectance (TDTR) for thermal property characterization of bulk and thin film materials. *Journal of Applied Physics* **2018**, *124*, 161103.

[2] Kang, K.; Koh, Y. K.; Chiritescu, C.; Zheng, X.; Cahill, D. G. Two-tint pump-probe measurements using a femtosecond laser oscillator and sharp-edged optical filters. *Review of Scientific Instruments* **2008**, *79*, 114901.

[3] Olson, D. H.; Gaskins, J. T.; Tomko, J. A.; Opila, E. J.; Golden, R. A.; Harrington, G. J.; Chamberlain, A. L.; Hopkins, P. E. Local thermal conductivity measurements to determine the fraction of α-cristobalite in thermally grown oxides for aerospace applications. *Scripta Materialia* **2020**, *177*, 214–217.

[4] Cahill, D. G. Analysis of heat flow in layered structures for time-domain thermoreflectance. *Review of scientific instruments* **2004**, *75*, 5119–5122.

[5] Schmidt, A. J.; Chen, X.; Chen, G. Pulse accumulation, radial heat conduction, and anisotropic thermal conductivity in pump-probe transient thermoreflectance. *Review of Scientific Instruments* **2008**, *79*, 114902.

[6] Hopkins, P. E.; Serrano, J. R.; Phinney, L. M.; Kearney, S. P.; Grasser, T. W.; Harris, C. T. Criteria for cross-plane dominated thermal transport in multilayer thin film systems during modulated laser heating. *Journal of Heat Transfer* **2010**, *132*.

[7] Hoque, M. S. B.; Koh, Y. R.; Braun, J. L.; Mamun, A.; Liu, Z.; Huynh, K.; Liao, M. E.; Hussain, K.; Cheng, Z.; Hoglund, E. R., et al. High In-Plane Thermal Conductivity of Aluminum Nitride Thin Films. *ACS Nano* **2021**, *15*, 9588–9599.

[8] Olson, D. H.; Avincola, V. A.; Parker, C. G.; Braun, J. L.; Gaskins, J. T.; Tomko, J. A.; Opila, E. J.; Hopkins, P. E. Anisotropic thermal conductivity tensor of β-Y2Si2O7 for orientational control of heat flow on micrometer scales. *Acta Materialia* **2020**, *189*, 299–305.

[9] Braun, J. L.; Olson, D. H.; Gaskins, J. T.; Hopkins, P. E. A steady-state thermoreflectance method to measure thermal conductivity. *Review of Scientific Instruments* **2019**, *90*, 024905.

[10] Touloukian, Y.; Powell, R.; Ho, C.; Klemens, P. Thermal Conductivity: Nonmetallic Solids volume 2 of Thermophysical Properties of Matter Eds YS Touloukian. *CY Ho (New York: IFI/Plenum) pp* **1970**, 182–193.

[11] Wilson, R.; Cahill, D. G. Anisotropic failure of Fourier theory in time-domain thermoreflectance experiments. *Nature communications* **2014**, *5*, 1–11.

[12] Wilson, R.; Cahill, D. G. Limits to Fourier theory in high thermal conductivity single crystals. *Applied Physics Letters* **2015**, *107*, 203112.

[13] Chen, L.; Braun, J. L.; Donovan, B. F.; Hopkins, P. E.; Poon, S. J. Ballistic transport of long wavelength phonons and thermal conductivity accumulation in nanograined silicon-germanium alloys. *Applied Physics Letters* **2017**, *111*, 131902.

[14] Parker, W.; Jenkins, R.; Butler, C.; Abbott, G. Flash method of determining thermal diffusivity, heat capacity, and thermal conductivity. *Journal of applied physics* **1961**, *32*, 1679–1684.

[15] Schwartz, A. J.; Kumar, M.; Adams, B. L.; Field, D. P. *Electron backscatter diffraction in materials science*; Springer, 2009; Vol. 2.

[16] Engler, O.; Randle, V. *Introduction to texture analysis: macrotexture, microtexture, and orientation mapping*; CRC press, 2009.